

Article

Influence of Luminescent Properties of Powders on the Fabrication of Scintillation Ceramics by Stereolithography 3D Printing

Lydia V. Ermakova, Valery V. Dubov , Rasim R. Saifutyarov, Daria E. Kuznetsova , Maria S. Malozovskaya, Petr V. Karpyuk, Georgy A. Dosovitskiy *  and Petr S. Sokolov 

Institute of Chemical Reagents and High Purity Chemical Substances of NRC “Kurchatov Institute” (IREA), Bogorodskiy val 3, 107076 Moscow, Russia

* Correspondence: george.dos@gmail.com

Abstract: Luminescent and scintillation ceramic materials with complex shapes, which can be created by stereolithography 3D printing, are of interest for special phosphor and detector applications. Starting powders for such ceramics may possess UV absorption bands; therefore, it is important to study the possible influence of the powders’ luminescent properties on the printing process. This paper deals with complex garnet oxides, $Y_3Al_5O_{12}$ and $Gd_3Al_2Ga_3O_{12}$ —well-known hosts for luminescent materials. The photopolymerization rates of slurries based on the luminescent powders produced by various chemical routes are studied, as well as available printing regimes. The slurries containing Ce-doped powders with a broad absorption band in UV have significantly lower photopolymerization rates compared to the undoped ones; a high Ce doping virtually hinders printing with layers thicker than 25–50 μm . Furthermore, the choice of powder synthesis method is shown to influence the printing process. Slurries with Tb-doped powder, with absorption lines at shorter wavelengths, have good photopolymerization activity, close to that of the undoped powder, and can be printed with layer thicknesses of 25–100 μm .



Citation: Ermakova, L.V.; Dubov, V.V.; Saifutyarov, R.R.; Kuznetsova, D.E.; Malozovskaya, M.S.; Karpyuk, P.V.; Dosovitskiy, G.A.; Sokolov, P.S.

Influence of Luminescent Properties of Powders on the Fabrication of Scintillation Ceramics by Stereolithography 3D Printing. *Ceramics* **2023**, *6*, 43–57. <https://doi.org/10.3390/ceramics6010004>

Academic Editor: Gilbert Fantozzi

Received: 29 November 2022

Revised: 23 December 2022

Accepted: 3 January 2023

Published: 7 January 2023



Copyright: © 2023 by the authors. Licensee MDPI, Basel, Switzerland. This article is an open access article distributed under the terms and conditions of the Creative Commons Attribution (CC BY) license (<https://creativecommons.org/licenses/by/4.0/>).

Keywords: 3D printing; cerium; garnet oxide; luminescence; phosphor; scintillator; stereolithography; terbium

1. Introduction

Garnet oxides doped with lanthanides are a group of widely used luminescent materials. Ce-doped $Y_3Al_5O_{12}$ (YAG:Ce) is an established LED phosphor [1,2]. YAG doped with Nd, Yb, or Er is widely applied in solid-state lasers [3–5]. Garnet oxides are scintillators with existing or anticipated applications in areas such as space measurements [6], medical and general X-ray imaging [7–9], and high-energy physics [10,11]. $Gd_3Al_2Ga_3O_{12}$ doped with Ce^{3+} activator (GAGG:Ce) is a relatively novel but well-established scintillator with competitive characteristics—a high density of about 6.63 g/cm³, main scintillation decay component below 100 ns and light yield of 40–60 kph/MeV [12–14]. It can be produced in the form of both single crystals [12–14] and translucent or transparent ceramics [15]. Tb-doped $(Gd,Y)_3(Al,Ga)_5O_{12}$ garnets (GYAGG:Tb) have slow luminescence decay kinetics in the order of milliseconds, which restricts their use in modern photon-counting applications. However, their light yield was shown to be very high, which makes this group of materials interesting for the transformation of radiation to light in converters for nuclear batteries or cathodoluminescent phosphors [16–18].

Luminescent ceramics could have advantages compared to single crystals if they can be produced more cheaply, or if any special requirements exist regarding the material’s shape or composition, e.g., in order to make a composite [19,20]. The fast development of additive manufacturing methods, i.e., 3D printing, allows for the fabrication of ceramic objects of complex shapes, which are unachievable using classical pressing or casting approaches.

Example application areas of such ceramics include bone surgery and engineering [21–23]. Construction materials were the first type of material for which additive manufacturing approaches were developed, but interest in functional materials has been increasing. A possible application of 3D-printed scintillators is as a flow-through detector of radioactive species in liquid media [24]. A metascintillator is another novel material concept, which requires a dense solid material with multiple channels with diameters of about 100–200 μm . This would serve as a heavy host, which should contain a fast component, e.g., in the form of nanoparticles [25–27]. It is essential to be able to try various geometrical host parameters in the development stage, which makes 3D printing an even more suitable approach.

Fe-containing garnet compounds, such as the well-known $\text{Y}_3\text{Fe}_5\text{O}_{12}$ (YIG), or more complex oxides, such as $\text{Y}_3\text{Al}_{5-x}\text{Fe}_x\text{O}_{12}$ and $\text{Gd}_3\text{Al}_{5-x}\text{Fe}_x\text{O}_{12}$ [28–31], are a related group of materials with various magnetic properties, which have applications in spintronics and magneto-optics. Most applications imply a thin-film form for the materials [28], but some compounds could have a polycrystalline form [29] for which 3D printing could be a formation technique, creating new possible applications.

Various additive manufacturing techniques were used to produce transparent or translucent garnet ceramics. Extrusion-based 3D printing and free sintering were used to make transparent YAG in [32]. YAG/YAG:Nd all-ceramic composites, as well as YAG:Lu and YAG:Gd ceramics, were fabricated by a combination of direct ink-writing, vacuum sintering, and hot isostatic pressing, as described in [33].

One of the most frequently developed methods of 3D printing that is suitable for mass application, stereolithography, provides one of the best spatial resolutions, with an acceptable building speed. Routine printers allow for a voxel (a minimal building volume, 3D pixels) lateral size in the range of 30–80 μm and a height in the range of 10–100 μm . The high spatial resolution of the fabricated object is an important requirement for such applications, as mentioned above. It should be noted that the practically achievable geometrical element size that could be built using this technique contains several voxels. The stereolithography method consists of the layer-by-layer polymerization of a photocurable slurry, as a result of its illumination with UV light according to a desired pattern, leading to layer-by-layer object formation. During the digital light processing (DLP) modification of the method, which is applied in this work, the source of light is a digital UV projector. To form a ceramic green body, the compound should contain the desired source powder, i.e., a slurry with a high powder load should be prepared, based on a photopolymerizable binder [34]. Oxide powders always scatter a projector's light, which influences the printing process; however, tuning the printing conditions and the slurry composition can achieve results close to those that could be achieved by printing purely with plastic [21,35–37]. Furthermore, powders with UV-excited luminescence or an absorption band in that region may partially absorb the light. One may expect this to significantly influence the volume and dynamics of the curing process, thus affecting the printing.

This problem has only been tackled in a few publications [38–43]. Adding yellow and red pigments of Pr- and Fe-doped ZrSiO_4 , respectively, to a zirconia-based slurry, leads to a decrease in cure depth and excessive width; as a result, exposure had to be increased in order to successfully print colored articles [38]. The authors of [39] report that adding CoCl_2 to an alumina-doped zirconia slurry led to an improvement in DLP-printed green bodies and ceramics; however, this was not directly linked to the slurry coloring. Ceria-stabilized zirconia-based composites were recently printed by laser [40] and DLP stereolithography [41,42]. Ceria-doped zirconia was shown to display a significant absorbance at 340–405 nm [40–42], which could be overcome by choosing the illumination wavelength [36] or preparation of a special slurry formulation [42]. A recent paper reported on the dependence of a polymerized layer thickness vs. laser power (wavelength not specified) for SLA-printing from ZrO_2 -based slurries, colored by additions of Co_3O_4 , Ce_2O_3 , and Er_2O_3 [43]. With the increase in the colorant content, a higher laser power was required to achieve the same curing depth.

Several works deal with luminescent garnets fabricated by stereolithographic methods. YAG:Yb laser ceramics were demonstrated using stereolithography and free sintering (SiO₂ was added as a sintering aid) [44]; it should be noted that both the absorption and emission of YAG:Yb are in the IR region [45], so they are not supposed to influence the printing process. The authors of [46] used two-phonon stereolithography to create micron-resolution YAG:Nd objects with laser properties. Although YAG:Nd has absorption bands in the near-UV region [47], the printing ink contained chlorides of the elements constituting the abovementioned work, and there was no luminescent garnet phase. Ce-doped garnets have broad absorption bands in near-UV and blue spectral regions [2]; nevertheless, a YAG:Ce scintillator was fabricated using DLP stereolithography, and its properties were no worse than those of the compound obtained using classical routes [48]. The use of laser SLA stereolithography for the production of YAG:Ce/Al₂O₃ ceramics was demonstrated in [49]. However, the positions of absorption bands depend on the exact composition of the garnet, since Ce³⁺ luminescence properties are strongly influenced by its local surroundings [50]. Therefore, the GAGG:Ce slurry was expected to perform differently, and this was studied in the current work. Tb-doped GAGG powder was used as another potentially interesting printing material with narrow absorption bands in the UV region.

High-quality powder is an important prerequisite for high-density ceramics. A coprecipitation approach was chosen in this work. This was proven to yield high-quality garnet powders, which could be sintered to transparency if the synthesis conditions are properly optimized [51,52]. Homogeneous precipitation was chosen as an alternative approach, allowing for the production of powder with low agglomeration and high sinterability [53].

We studied the photopolymerization behaviors of slurries based on two promising scintillator compositions, GAGG:Ce and GAGG:Tb, as well as YAG:Ce, as a well-known material. The starting powders were synthesized in-house using different techniques. The DLP 3D-printing method was used to shape the ceramics. This is one of the most widely available techniques for a wide range of researchers. The powder properties' influence on the printing process and results is reported.

2. Materials and Methods

2.1. Starting Materials

The powders of Gd_{2.988}Ce_{0.012}Al₂Ga₃O₁₂ (GAGG:Ce) compositions were synthesized by two approaches—coprecipitation (CP) and homogeneous precipitation (HP). The Y₃Al₅O₁₂ (YAG *white*), Y_{2.97}Ce_{0.03}Al₅O₁₂ (YAG:Ce), Gd_{2.97}Ce_{0.03}Al₂Ga₃O₁₂ (GAGG:Ce+), Gd_{2.88}Tb_{0.12}Al₂Ga₃O₁₂ and Gd₃Al₂Ga₃O₁₂ (GGAG *white*) powders were synthesized using only the coprecipitation method. Powder synthesis, following the CP approach, included the preparation of a nitrate solution, containing all the necessary elements, with a total metal ion concentration of 1 mol/L. This was slowly added to an ammonium hydrogen carbonate (NH₄HCO₃) solution (pH was maintained at 6.9–7.0 to ensure full precipitation), before filtering and calcining the precipitate that was formed. Some additional synthesis details are given in [54]. The homogeneous precipitation approach was adopted from [53] and included the preparation of a nitrate solution with all metal ions at a total concentration of 0.05 mol/L, where ammonium sulfate ((NH₄)₂SO₄) was added to a concentration of 0.06 mol/L, and carbamide ((NH₂)₂CO) with a 40-fold molar excess relative to metal ions. Then, the reaction volume was held at 90 °C for 5 h and cooled down; the pH of the resulting suspension was approximately 7.5. After the synthesis, the powders were calcined at temperatures of 1200–1300 °C, depending on the composition and synthesis route. Finally, the powders were milled in a planetary ball mill (Retsch, PM100), using alumina jars and balls, in pure isopropyl alcohol for 60 min. Powder abbreviations, compositions, and calcining temperatures are given in Table 1.

Table 1. Powders used in this study.

Abbreviation	Synthesis Approach	Composition	Calcining Temperature (°C)
YAG <i>white</i>	Coprecipitation	Y ₃ Al ₅ O ₁₂	1300
YAG:Ce CP	Coprecipitation	Y _{2.97} Ce _{0.03} Al ₅ O ₁₂	1300
GAGG:Ce 1200 HP	Homogeneous precipitation	Gd _{2.988} Ce _{0.012} Al ₂ Ga ₃ O ₁₂	1200
GAGG:Ce 1300 HP	Homogeneous precipitation	Gd _{2.988} Ce _{0.012} Al ₂ Ga ₃ O ₁₂	1300
GAGG:Ce CP	Coprecipitation	Gd _{2.988} Ce _{0.012} Al ₂ Ga ₃ O ₁₂	1200
GAGG:Ce+ CP	Coprecipitation	Gd _{2.97} Ce _{0.03} Al ₂ Ga ₃ O ₁₂	1200
GAGG:Tb CP	Coprecipitation	Gd _{2.88} Tb _{0.12} Al ₂ Ga ₃ O ₁₂	1200
GAGG <i>white</i>	Coprecipitation	Gd ₃ Al ₂ Ga ₃ O ₁₂	1200

All powders had good sinterability. This was tested by creating a cylindrical pellet from each powder with a diameter of 20 mm and height of 1 mm by dry uniaxial pressing at 64 Mpa, followed by sintering at 1600 °C in air. The relative green density of such pellets was around 50% and that of sintered ceramics was no lower than 97%.

2.2. Slurry Preparation and 3D Printing

1,6-Hexanediol diacrylate (HDDA, 80%, Sigma-Aldrich, St. Louis, MI, USA) was used as a reactive binder. This is a widely used monomer for the formation of stereolithography-based ceramics due to its low viscosity and acceptable curing kinetics [34]. UV-photoinitiator TPO-L (BASF, Ludwigshafen, Germany), with 1 wt.% of HDDA, was added to enable radical polymerization. BYK w9010 (BYK-Chemie GmbH, Wesel, Germany) was used as a colorless rheological additive with a dosage of ~2 mg/m² [36]. The slurries were prepared by mixing all organic components and subsequently adding one of the powders in small portions up to a load of 30 vol.%.

The viscosity measurements were performed using a Physica MCR-52 rheometer (Anton Paar, Graz, Austria) in a shear rate range from 1 to 200 s⁻¹ and a parallel-plate geometry of 20.0 °C. The disk diameter was 25 mm, and the gap was 0.5 mm.

Three-dimensional printing, as well as polymerization depth measurements, were performed using an Ember DLP 3D printer (Autodesk, Mill Valley, CA, USA) at ambient room conditions, with a temperature of 22–26 °C and humidity of 20–35%. The illumination spectrum of the printer's projector ranged from 385 to 425 nm, peaking at 405 nm. Its radiation power was measured with UV-light-meter Model 222 (G&R Labs, Santa Clara, CA, USA) and amounted to 16.5 mW/cm². The nominal in-plane resolution of the 3D printer was 50 µm [35–37].

Two main 3D models were used in this work. The first one was a thin-wall tube with holes of about 400 µm [36]. Its size was 3.8 × 3.8 × 6.0 mm. The second one was a flat net-shaped body with a size of 12.25 × 13.00 × 1.0 mm. This was designed using the FreeCAD software ver. 0.17 (see the .stl file in File S1).

Debinding of the green bodies was performed by continuously heating them to 550 °C at a rate of 1 °C/min in air. Ceramics were sintered at either 1600 °C for 2 h in air or at 1650 °C for 4 h in oxygen flow in chamber LHT 02/17 (Nabertherm) and tube RHTH 80-300/18 (Nabertherm) furnaces, respectively.

2.3. Characterization Techniques

The phase compositions of the powders were examined using X-ray powder diffraction on a D2 Phaser (Bruker, Billerica, MA, USA), with CuKα_{1,2} radiation. Particle size distributions were measured using laser diffraction on a MasterSizer 2000 (Malvern, PA, USA) with a water-filled dispersing unit Hydro G (see Supplementary Materials for details). The specific surface values of the powders were determined according to the capillary nitrogen condensation method using BET model values on NOVAtouch NT LX (Quantachrome Instruments, Anton Paar Group, Graz, Austria). The powder particles' morphology and ceramics' cross-sections were studied using a JSM 7100F (Jeol, Japan) scanning electron microscope in secondary electron mode at an accelerating voltage of 10 kV. Low-magnification images of the green bodies and sintered ceramics were taken by SEM SU1510 (Hitachi, Japan) in secondary electrons and in back-scattering mode at 3–7 kV. Photographs of the

green bodies and ceramics were obtained by the microscopes MET 5C and SM0745 (Altami Ltd., St. Petersburg, Russia).

The thermogravimetry and differential heat flow (DSC) of the cured powder-loaded slurries were performed using SDT Q600 (TA Instruments, New Castle, DE, USA) at a constant heating rate of 2.5 °C/min, from room temperature to 550 °C with airflow.

Steady-state photoluminescence emission and excitation spectra were measured using Fluorat-02-Panorama (Lumex, St. Petersburg, Russia) spectrofluorimeter with a xenon lamp light source and optical fiber measurement attachment for powders. Scintillation light yield was measured using photomultiplier R 1828-01 (Hamamatsu, Japan) coupled with signal processing equipment of NIM standard (ORTEC, Atlanta, GA, USA). Pulse height spectra of ^{137}Cs source of 662 keV gamma-quanta were taken with the measured samples, as well as with a reference GAGG:Ce single crystal (JCS Fomos-Materials) with a light yield of 28.5 kph/MeV.

3. Results and Discussion

SEM images of the powders are given in Figure 1. One can see that the powders synthesized via co-precipitation have crystallites with sizes of about 100–150 nm, and the powders synthesized via homogeneous precipitation were in the range 200–1500 nm, with a large fraction of particles >1 μm . All the powders contained dominant cubic garnet phases, PDF # 46-0448 for GAGG and PDF # 33-0040 for YAG, according to the X-ray powder diffraction (see Supplementary Materials, Figure S1). Both the GAGG HP powders contained an impurity phase of Gd_3GaO_6 (PDF # 89-6631) or some isostructural Gd_3GaO_6 -based solid solution, and all the CP powders were phase-pure.

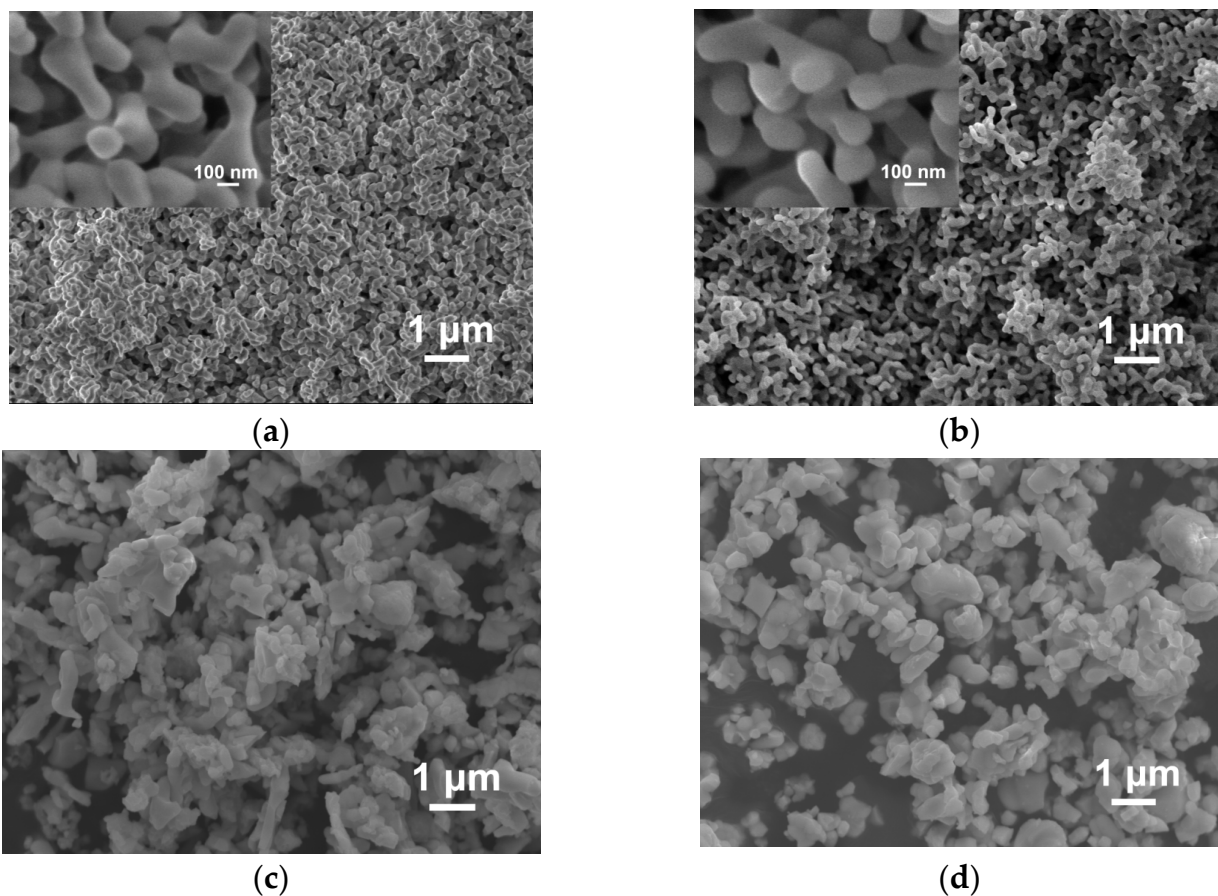


Figure 1. Cont.

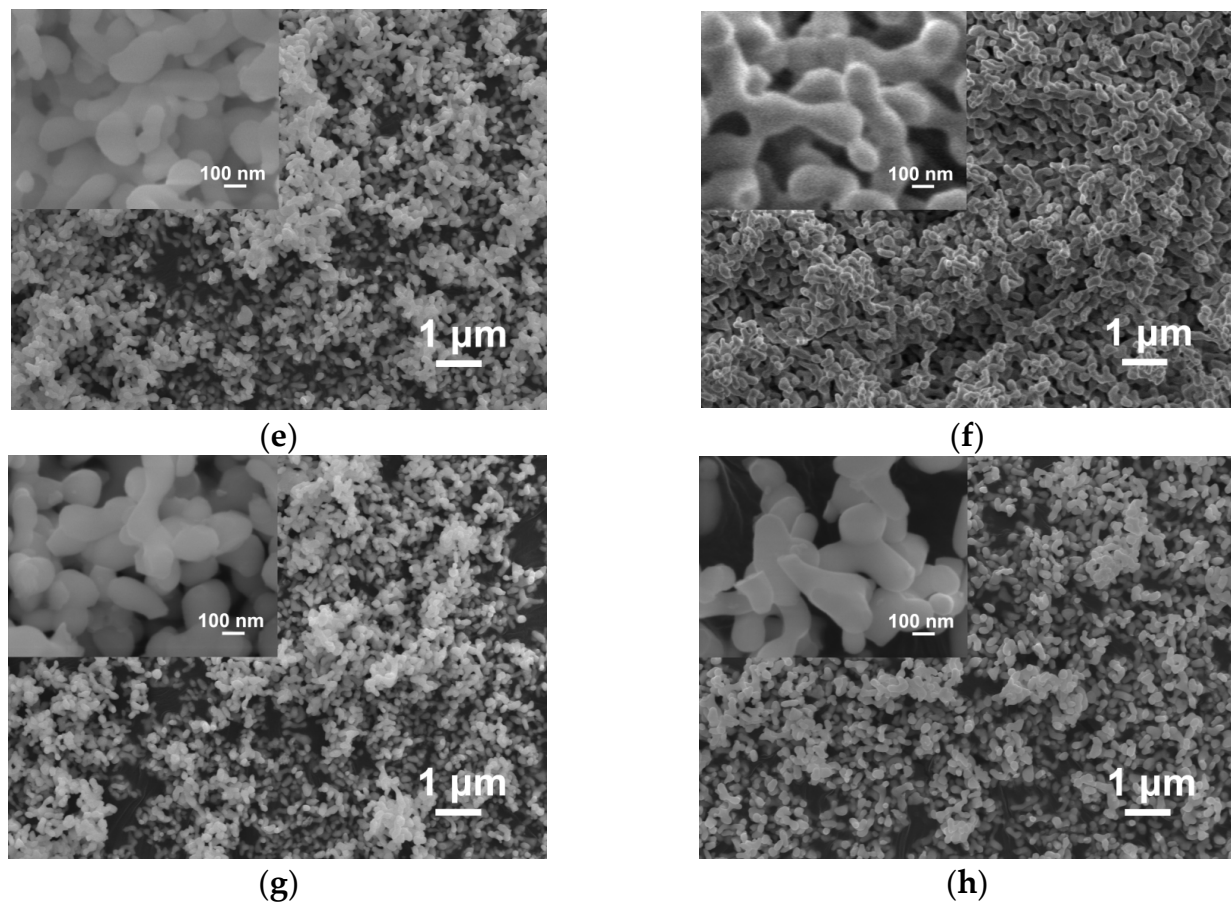


Figure 1. SEM images of the powders used: (a) YAG *white*, (b) YAG:Ce CP, (c) GAGG:Ce 1200 HP, (d) GAGG:Ce 1300 HP, (e) GAGG:Ce CP, (f) GAGG:Ce+ CP, (g) GAGG:Tb CP, (h) GAGG *white*.

The powders' specific surface values (BET) and the characteristic percentile values for their particle size distributions are given in Table 2. The mean primary particle sizes of the CP powders, estimated using their specific surface values, were within the range 150–200 nm (assuming a spherical shape of the particles), which corresponds to the SEM observations. The same estimation for the HP powders leads to values of 200–300 nm, which is smaller than the size observed by SEM. A possible reason for this difference is the internal porosity of the HP powders. Particle size distributions for the CP powders contain two fractions according to a laser diffraction of about 100–150 nm (primary particles) and about 1 μm (agglomerates). The HP powders' distributions contain a single peak near 1 μm with a broad distribution, possibly corresponding to primary particles. All the CP powders have d_{90} values below 1.2 μm (i.e., 90% of the particles or aggregates are smaller than this value), and the HP powders are below 2.5 μm . Particle size distributions are given in Figure S2 of the Supplementary Materials.

Table 2. Specific surface areas and percentile values of particle size distributions for the powders used in this study.

Powder	BET Specific Surface, m^2/g	d_{10} , μm	d_{50} , μm	d_{90} , μm
YAG <i>white</i>	9.7	0.11	0.19	0.88
YAG:Ce CP	10	0.11	0.18	0.64
GAGG:Ce 1200 HP	5.2	0.46	1.00	2.10
GAGG:Ce 1300 HP	3.6	0.65	1.22	2.27
GAGG:Ce CP	7.3	0.10	0.18	1.00
GAGG:Ce+ CP	4.3	0.10	0.16	0.36
GAGG:Tb CP	8.2	0.11	0.35	1.21
GAGG <i>white</i>	—	0.10	0.34	1.06

Photoluminescence excitation spectra of Ce-doped GAGG powders show strong absorption bands, with maxima at 345 and 445 nm (Figure 2). Most of this light is re-emitted at higher wavelengths, but the emission bands for these powders are in the 470–600 nm range, which is beyond the absorption band of the TPO-L photoinitiator. Therefore, the absorbed light does not contribute to photopolymerization. A 405 nm LED emission spectrum, like the one that is used as a light source in an Ember 3D printer, is also shown in the figure. One can see that although the 460 nm YAG:Ce excitation band has a higher peak intensity, GAGG:Ce bands have a larger overlap with the LED emission spectrum, as well as with the absorption spectrum of TPO-L. However, the excitation spectrum of GAGG:Tb powder does not overlap with the LED emission spectrum at all.

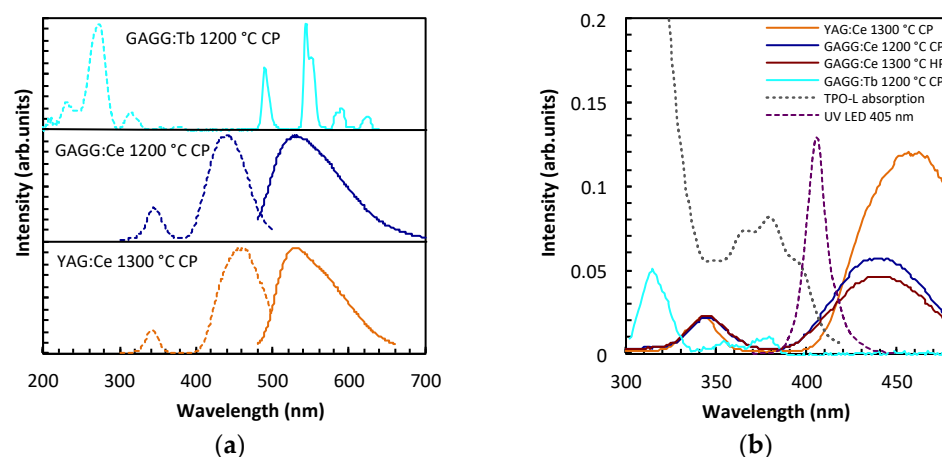


Figure 2. (a) Photoluminescence excitation and emission spectra for YAG:Ce, GAGG:Ce, and GAGG:Tb, all normalized by the most intensive peak. (b) Photoluminescence excitation spectra for GAGG:Ce, YAG:Ce, and GAGG:Tb powders, as measured, with corresponding synthesis routes and thermal treatment temperatures specified. TPO-L absorption spectrum (adapted from [55]) and typical 405 nm LED spectrum are given in arbitrary intensity scales related to the powder's spectra.

Photopolymerization curves are given in Figure 3. One can see that the undoped powders fabricated by coprecipitation, both YAG *white* and GAGG *white*, as well as the GAGG:Tb CP powder, have shown close polymerization thicknesses at an equivalent dose, with the highest results among the studied powders. The slight difference between the polymerization curves for suspensions with white YAG and GAGG powders can be explained by their different densities (4.56 g/cm³ for YAG *versus* 6.63 g/cm³ for GAGG) and different refractive indexes ($n_{405} = 1.78$ for YAG *versus* $n_{405} = 1.95$ for GAGG). The penetration depth, D_p , and critical energy dose, E_c , of the slurries with different powders were calculated based on the Jacobs Equation (1), derived from the Beer–Lambert law, and are given in Table 3. C_p stands for curing depth at a given dose.

$$C_p = D_p \ln(E/E_c) \quad (1)$$

The doping of YAG by 0.03 formula units (f.u.) of Ce and doping of GAGG by 0.012 f.u. of Ce caused a decrease in a polymerized layer thickness. Additional GAGG:Ce+ CP coprecipitated powder, containing 0.03 f.u. of Ce (all the other characteristics were close to the other GAGG:Ce CP powders), was tested; this caused a further decrease in polymerized layer thickness (Figure 3b). Among the Ce-doped powders, the polymerizability decreases with the increase in excitation band intensity in the row GAGG:Ce 1200 HP, GAGG:Ce 1300 HP, GAGG:Ce CP. This correlates with the fact that the garnet phase is formed at higher temperatures in homogeneously precipitated powders, as evidenced by XRD.

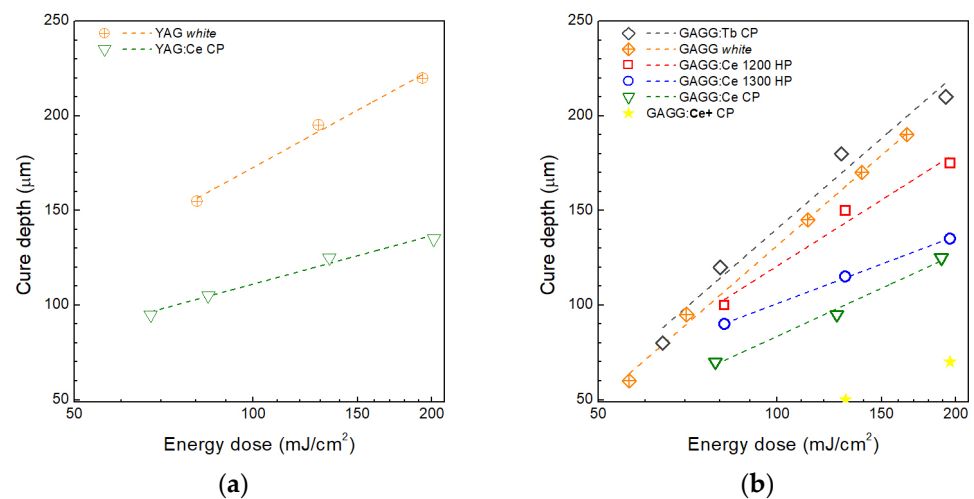


Figure 3. The thickness of a polymerized layer at different energy doses for slurries loaded with (a) YAG:Ce, (b) GAGG:Ce/Tb powders. The dash lines represent the Jacobs equation (Beer–Lambert law) fitted with parameters from Table 3.

Table 3. Calculated penetration depth (D_p) and critical energy (E_c) of HDDA/w9010/TPO-L slurries with 30 vol.% of different powders.

Powder	D_p (μm)	E_c (mJ/cm^2)	R^2
YAG <i>white</i>	81 (16)	17 (7)	0.96
YAG:Ce CP	37 (3)	5 (1)	0.99
GAGG:Ce 1200 HP	86 (13)	24 (6)	0.98
GAGG:Ce 1300 HP	51 (1)	14 (1)	0.99
GAGG:Ce CP	63 (6)	26 (4)	0.99
GAGG:Tb CP	118 (13)	30 (5)	0.97
GAGG <i>white</i>	118 (4)	33 (1)	0.99

The polymerization depth of a slurry depends on the organic binder, viscosity, powder load, particle size distribution, and residual gas caught inside the slurry [21,34–37]. However, if both the organic constituents and preparation technique are unified, the main factor causing different slurry behaviors is the filling powder. The powder can either scatter or absorb light in a suspension during the photopolymerization process. The light scattering is mostly determined by the microstructure, particle size distribution, and differences in the refractive indexes of the powder and the resin. These factors were equal or close for the powders under study. Therefore, the powders' luminescent properties are the main factors influencing the slurries' properties.

All suspensions in this work had viscosities in the close range of 0.3–0.5 Pa·s at 50 s⁻¹. This value is sufficiently low to provide a good slurry flow, which is suitable for printing on machines with the simplest designs. The representative viscosity and shear stress curves are given in the Supplementary Materials (Figure S3).

A net-shaped tube element was chosen as the model printing object to study how a starting powder influences the available printing conditions. The green bodies were printed, debinded, and sintered; exemplary stereomicroscopic images are given in Figure 4. The thermal decomposition of polymerized organic binder in the green bodies was typical for acrylate-based polymers and took place below 500 °C. Representative thermogravimetry curves are given in the Supplementary Materials (Figure S4). The debinding behaviors of GAGG:Ce CP and YAG:Ce are generally similar; however, a slight difference was observed in white (undoped and Tb-doped) powders. The small printing volumes allowed us to use a simplified binder burnout regime. The densities of all YAG ceramics (3D-printed and pellets) were no less than 4.4 g/cm³, and GAGG was no less than 6.5 g/cm³. The grain

sizes of the ceramics were in the range of 1–2 μm , and the samples contained few pores; a typical cross-section is presented in Figure S5 of the Supplementary Materials.

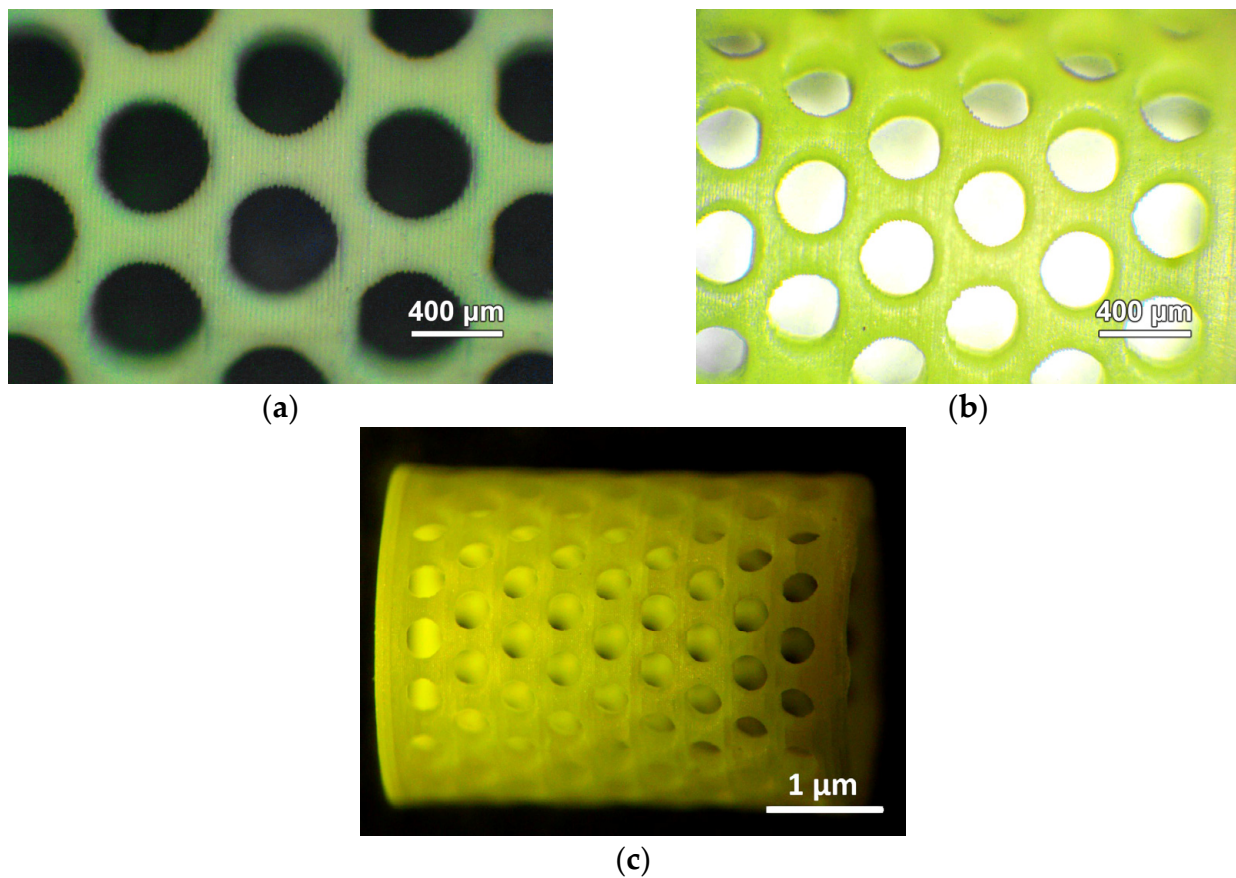


Figure 4. Optical image of (a) green body and (b,c) sintered ceramics from GAGG:Ce+ CP powder, fabricated on a 25 μm layer.

YAG:Ce ceramic tablets (~ 1 mm thick) after sintering in both air and oxygen atmospheres are opaque. Tablets of GAGG:Ce ceramics are barely transparent after sintering in air; however, in an oxygen atmosphere, the transparency clearly improves and the total transmittance reaches 47%. This difference in the behavior of the garnet ceramics of two compositions can be explained by the different melting points of YAG:Ce and GAGG:Ce (1970 $^{\circ}\text{C}$ vs. 1850 $^{\circ}\text{C}$, respectively).

Both the YAG:Ce and GAGG:Ce ceramics obtained by 3D printing are opaque, perhaps due to the relatively low filling in the green bodies (~ 30 vol.% vs. 50 vol.% for pressed tablets). Thus, one way to increase ceramics' transparency could be an increase in garnet powder load of a suspension to at least 45–50 vol.%. This may require the use of more reactive monomer(s) or/and UV photoinitiator(s) [42].

The different curing doses required for layer polymerization mean that longer exposition times are needed for each layer. This practically limits the printing layer thickness, as the long exposition times needed for DLP printing led to printed objects sticking to the bottom window of the printing vat, which is made of polydimethylsiloxane and covered with a FEP film. This causes either damage to the printed object or the quick degradation of the vat window. At the same time, too thin a printing layer, for example, 10 μm , increases the requirements for the printer's precise mechanical alignment, which makes the formation process less stable. The doses required for printing with slurries containing various powders were estimated based on the printing results and are summarized in Table 4.

Table 4. Values of the minimum irradiation doses (in mJ/cm²) necessary to polymerize a given layer of a suspension with various fillers.

Layer Thickness	Powder			
	YAG:Ce CP	YAG <i>white</i>	GAGG:Ce 1200 HP	GAGG:Ce 1300 HP
25 μm	—	—	—	Dose:50
50 μm	Dose: 50	—	Dose: 80	Dose:75
75 μm	Dose: 120	—	Dose: 130	Dose: 110
100 μm	Printing unavailable	Dose: 90	Dose: 145	Dose: 160

Layer Thickness	Powder			
	GAGG:Ce CP	GAGG:Ce+ CP	GAGG:Tb CP	GAGG <i>white</i>
25 μm	Dose: 80	Dose: 130	Dose: 56	—
50 μm	Dose: 100	Printing unavailable	Dose: 70	—
75 μm	Dose: 140	Printing unavailable	Dose: 80	—
100 μm	Dose: 190	Printing unavailable	Dose: 110	Dose: 110

The larger the overlap between a photoluminescence excitation peak in a powder and the LED emission band, the higher the required illumination dose and the thinner the layer available for printing. Slurries based on undoped powders allow for the use of 100 μm layers or printing. High-quality ceramics can be obtained at a layer thickness of 100 μm from GAGG:Tb and GAGG:Ce CP powders, as well as from the HP powders. The thickest printing layer available for YAG:Ce (0.03 f.u. Ce) powder was 75 μm, and 25 μm was the maximum thickness for GAGG:Ce+ CP (0.03 f.u. Ce) powder. SEM images of green bodies and ceramics fabricated with printing layers of 50 μm and 100 μm are given in Figures 5 and 6.

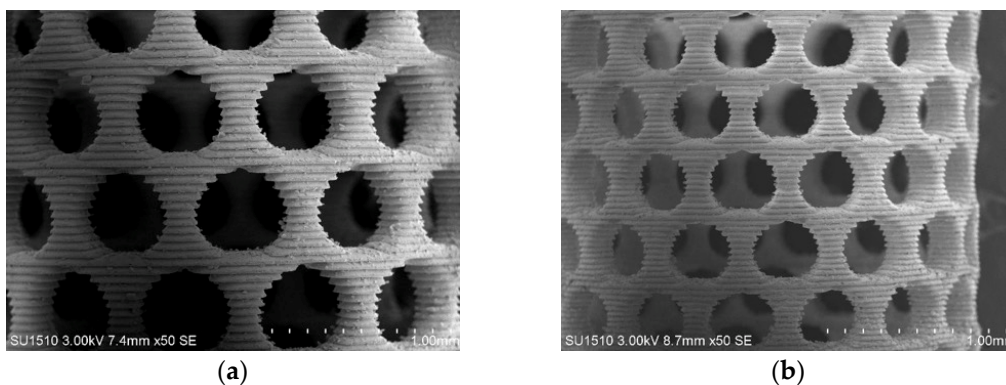


Figure 5. SEM image of (a) green body and (b) sintered ceramics from GAGG:Ce CP powder, fabricated at 50 μm layer.

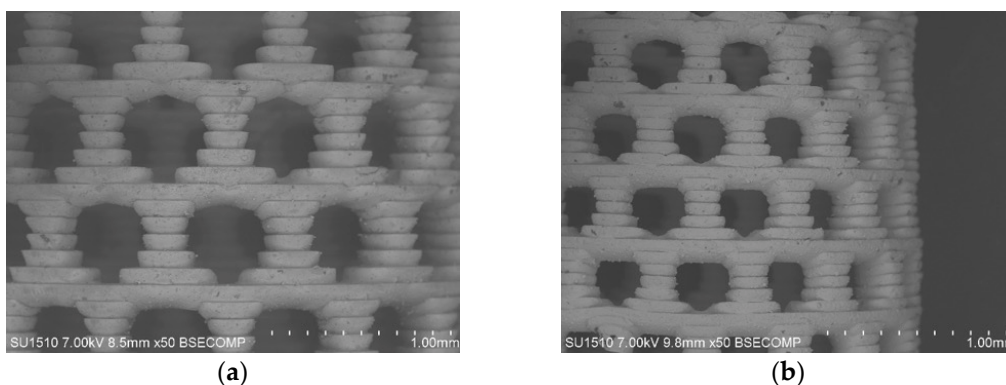


Figure 6. SEM image of (a) green body and (b) sintered ceramics from GAGG:Tb CP powder, fabricated with a 100 μm layer.

Stereolithography printing includes stages of slurry illumination (their duration is determined by the required illumination dose) and mechanical movement of the object being printed to allow for fresh building material to access the printing area. The latter stage takes time and is the main source of possible defects in printed objects (interlayer delamination, bubbles, etc.). Thus, a thicker printing layer allows for a faster and more reliable process when surface finish and fine details are not crucial.

According to the printing results, most green bodies did not show any cracks or delamination. However, after debinding and sintering, some of the samples printed with layer thicknesses of 25 and 50 μm had occasional defects. Overexposure to UV light or a non-optimized debinding process may have caused severe delamination in YAG *white* and GAGG *white* samples.

Model 1 is a relatively simple object to print due to its small cross-section. After optimizing the printing conditions, *Model 2* was printed (Figure 7). This was more complicated due to its increased cross-section, which means that it stuck more to the vat bottom during printing and required strong bonding to a building platform. Scintillation light yield was measured for this ceramic object and for a reference sample, comprising a flat tablet created using the same powder (Figure 8). Both ceramic samples demonstrated a similar scintillation light yield and were equal about half the value of a single crystal, i.e., ~ 14.2 kph/MeV. It is important to note that the scintillation light yield of a 3D-printed garnet ceramics was not inferior to that measured for a flat tablet, despite the fact that a phosphine-oxide photoinitiator and a phosphorus-containing rheological additive were used to create the former.

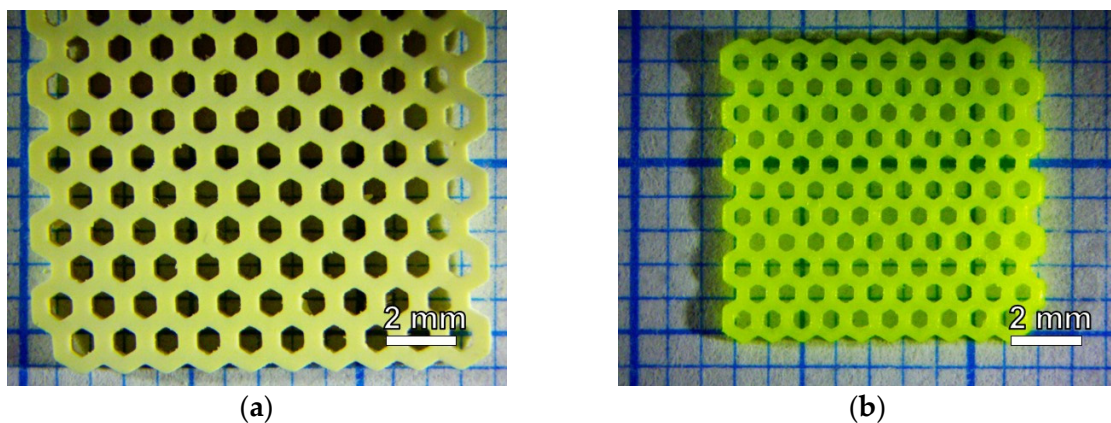


Figure 7. Optical image of (a) green body and (b) sintered ceramics from GAGG:Ce CP powder, fabricated with a 50 μm layer.

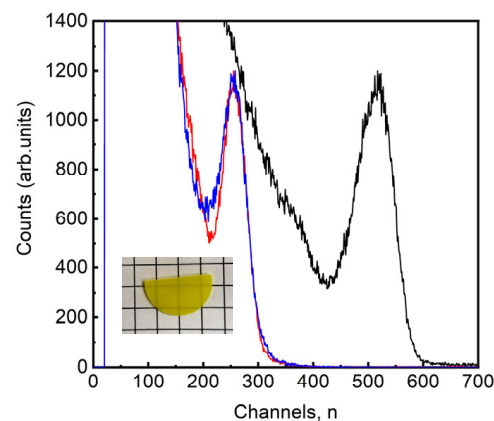


Figure 8. Light yield spectra of reference crystal (black line), GAGG:Ce CP ceramic tablet (red line), GAGG:Ce CP 3D printed ceramics (blue line), Inset: Ceramics of GAGG:Ce CP after sintering in oxygen atmosphere.

To test the printing conditions, additional models were printed from GAGG:Ce CP powders, forming orthogonal meshes with different cell sizes. The optical microscopy of the sintered ceramics samples with a wall thickness of ~200 μm and lattice period either 200 μm or 1 mm is presented in Figure S6 of the Supplementary Materials.

Thus, we demonstrated that the formation of GAGG:Ce scintillation ceramics using a desktop DLP 3D printer with a wavelength of 405 nm is possible (with a few limitations). A relatively low suspension solid load of 30 vol.% was chosen to compare all the powders under identical conditions. The maximum powder content varied across the used powders while maintaining an acceptable slurry viscosity because they had different morphologies and specific surface areas; the maximum content ranged up to 35 vol.%. A further increase in solid load could be achieved in three ways: (1) choosing powders with low specific surface area and uniform, sphere-like particles; (2) further testing and selecting dispersant(s) and polymerizable binder composition; (3) using a thicker slurry consistency (paste-like); however, the latter will require a different printer construction. A higher solid load, in its turn, could influence photopolymerization. From our results and previous experience, undoped or Tb-doped garnets could be printed from a 50 vol.% slurry, as the required illumination doses are far from marginal for 30 vol.% slurries. Another way to improve the photopolymerizing ability, if needed, is using more reactive mixtures of monomers and photoinitiators.

The use of printers with different illumination wavelengths could be considered. We believe that printing with Ce^{3+} -activated garnet powders (GAGG:Ce and YAG:Ce) using a commercial Lithoz 3D printer (working wavelength of 460 nm) will likely be difficult due to the strong absorption. Laser-based industrial SLA printers, e.g., Ceramaker 3DCeram, with a curing laser wavelength of 355 nm, may also have problems with cerium-doped powders [43]. Machines with a near-UV of 365 or 385 nm as a light source are probably better-suited to the printing of Ce^{3+} -activated garnet powder suspensions, as they fall within the narrow window of UV transparency for these garnets.

4. Conclusions

GAGG:Ce and GAGG:Tb ceramic net-shaped objects with submillimeter features—a wall thickness of 200–400 μm and round holes of 200–700 μm —were fabricated using DLP 3D-printing. It was shown that the luminescent properties of the starting powders, namely, the overlap of photoluminescence excitation band(s) with the 3D printer light source emission, are a detrimental factor in curing dynamics, which limits the available printing regimes. Therefore, thicker layers of YAG:Ce could be printed compared to GAGG:Ce with equivalent dopant concentrations. Powders obtained by homogeneous precipitation had a lower photoluminescence excitation band intensity and required a lower illumination dose to be printed with a given layer thickness compared to powders, synthesized by co-precipitation. To find a wide range of available printing parameters to obtain luminescent ceramics using DLP, one should either choose a printer with an appropriate light source, which does not overlap with powder absorption bands, or use powders with underdeveloped luminescent properties.

Supplementary Materials: The following supporting information can be downloaded at: <https://www.mdpi.com/article/10.3390/ceramics6010004/s1>, File S1—file *honeycombs.stl* with a 3D model used in this work; File S2—Figure S1: XRD patterns of the powders used in the work. Figure S2: Particle size distributions of the powders used in the work. Figure S3: Viscosity and shear stress vs. shear rate for the typical slurry used in the work. Figure S4: TG, DTG and DSC curves of the cured composites. Figure S5: SEM images of the cross-section of a typical 3D-printed ceramic sample. Figure S6: Optical microscopy images of sintered ceramics of additional printed geometries.

Author Contributions: Conceptualization, P.S.S., G.A.D. and D.E.K.; methodology, P.V.K. and V.V.D.; validation, P.S.S.; investigation, L.V.E., V.V.D., P.V.K., M.S.M. and R.R.S.; data curation, L.V.E.; writing—original draft preparation, G.A.D.; writing—review and editing, P.S.S. and L.V.E.; visualization, L.V.E., P.S.S. and G.A.D.; supervision, P.S.S. and G.A.D.; project administration, D.E.K. and G.A.D.; funding acquisition, G.A.D. All authors have read and agreed to the published version of the manuscript.

Funding: Analytical studies using X-ray diffraction and scanning electron microscopy methods were carried out using the scientific equipment of CKP NRC “Kurchatov Institute—IREA”, with the Russian Federation’s financial support, as represented by the Ministry of Education and Science of Russia, Agreement No. 075-15-2022-1157, dated 16.08.2022. Powder synthesis, optical characteristics’ measurements, slurry preparation, curing curve measurements, 3D printing and sintering were performed with the support of the grant of the Russian Science Foundation No. 22-13-00172, <https://rscf.ru/en/project/22-13-00172/>, in Institute of Chemical Reagents and High Purity Chemical Substances of NRC “Kurchatov institute”.

Institutional Review Board Statement: Not applicable.

Informed Consent Statement: Not applicable.

Data Availability Statement: Not applicable.

Acknowledgments: The authors are very grateful to A.E. Amelina (IREA) for providing the *stl*-model for 3D printing, A.S. Nartov (IREA) for the help with SEM, I.S. Komrotov (IREA) for the thermal analysis and S.I. Fedorchenko (IREA) for the viscosity measurements.

Conflicts of Interest: The authors declare no conflict of interest.

References

- Schlotter, P.; Schmidt, R.; Schneider, J. Luminescence conversion of blue light emitting diodes. *Appl. Phys. A-Mater.* **1997**, *64*, 417–418. [[CrossRef](#)]
- Smet, P.F.; Parmentier, A.B.; Poelman, D. Selecting conversion phosphors for white light-emitting diodes. *J. Electrochem. Soc.* **2011**, *158*, R37. [[CrossRef](#)]
- Kaminskii, A.A. Laser crystals and ceramics: Recent advances. *Laser Photonics Rev.* **2007**, *1*, 93–177. [[CrossRef](#)]
- Lupei, V.; Lupei, A.; Pavel, N.; Taira, T.; Ikesue, A. Comparative investigation of spectroscopic and laser emission characteristics under direct 885-nm pump of concentrated Nd: YAG ceramics and crystals. *Appl. Phys. B-Laser O.* **2001**, *73*, 757–762. [[CrossRef](#)]
- Kaminskii, A.A.; Balashov, V.V.; Cheshev, E.A.; Kopylov, Y.L.; Koromyslov, A.L.; Krokhin, O.N.; Kravchenko, V.B.; Lopukhin, K.V.; Shemet, V.V. High quality Y₃Al₅O₁₂ doped transparent ceramics for laser applications, role of sintering additives. *Opt. Mat.* **2017**, *71*, 103–108. [[CrossRef](#)]
- Iyudin, A.F.; Svertilov, S.I. Application of scintillation detectors in cosmic experiments. In *Engineering of Scintillation Materials and Radiation Technologies. ISMART 2018*; Korzhik, M., Gektin, A., Eds.; Springer Proceedings in Physics; Springer: Berlin/Heidelberg, Germany, 2019; Volume 227, pp. 165–185. [[CrossRef](#)]
- Lecoq, P.; Gektin, A.; Korzhik, M. *Inorganic Scintillators for Detector Systems. Particle Acceleration and Detection*; Springer: Berlin/Heidelberg, Germany, 2017; p. 408. [[CrossRef](#)]
- Yamamoto, S.; Nitta, H. Development of an event-by-event based radiation imaging detector using GGAG: A ceramic scintillator for X-ray CT. *Nucl. Instrum. Meth. A* **2018**, *900*, 25–31. [[CrossRef](#)]
- Ji, T.; Wang, T.; Li, H.; Peng, Q.; Tang, H.; Hu, S.; Yakovlev, A.; Zhong, Y.; Xu, X. Ce³⁺ doped yttrium aluminum garnet transparent ceramics for high-resolution X-ray imaging. *Adv. Opt. Mater.* **2022**, *10*, 2102056. [[CrossRef](#)]
- An, L.; Auffay, E.; Bettim, F.; Dall’Omo, F.; Gascon, D.; Golutvin, A.; Guz, Y.; Kholodenko, S.; Martinazzoli, L.; Mazorra De Cos, J.; et al. Performance of a spaghetti calorimeter prototype with tungsten absorber and garnet crystal fibres. *Nucl. Instrum. Meth. A* **2023**, *1045*, 167629. [[CrossRef](#)]
- Alenkov, V.; Buzanov, O.; Dosovitskiy, G.; Egorychev, V.; Fedorov, A.; Golutvin, A.; Guz, Y.; Jacobsson, R.; Korjik, M.; Kozlov, D.; et al. Irradiation studies of a multi-doped Gd₃Al₂Ga₃O₁₂ scintillator. *Nucl. Instrum. Meth. A* **2019**, *916*, 226–229. [[CrossRef](#)]
- Kamada, K.; Shoji, Y.; Kochurikhin, V.V.; Nagura, A.; Okumura, S.; Yamamoto, S.; Yeom, J.Y.; Kurosawa, S.; Pejchal, J.; Yokota, Y.; et al. Large size Czochralski growth and scintillation properties of Mg²⁺ co-doped Ce:Gd₃Ga₃Al₂O₁₂. *IEEE Trans. Nucl. Sci.* **2016**, *63*, 443–447. [[CrossRef](#)]
- Korzhik, M.; Alenkov, V.; Buzanov, O.; Fedorov, A.; Dosovitskiy, G.; Grigorjeva, L.; Mechinsky, V.; Sokolov, P.; Tratsiak, Y.; Zolotarjovs, A.; et al. Nanoengineered Gd₃Al₂Ga₃O₁₂ scintillation materials with disordered garnet structure for novel detectors of ionizing radiation. *Cryst. Res. Technol.* **2019**, *54*, 1800172. [[CrossRef](#)]
- Tamulaitis, G.; Vasilyev, A.; Korzhik, M.; Mazzi, A.; Gola, A.; Nargelas, S.; Vaitkevicius, A.; Fedorov, A.; Kozlov, D. Improvement of the time resolution of radiation detectors based on Gd₃Al₂Ga₃O₁₂ scintillators with SiPM readout. *IEEE Trans. Nucl. Sci.* **2019**, *66*, 1879–1888. [[CrossRef](#)]
- Zhu, Y.; Qian, S.; Wang, Z.; Guo, H.; Ma, L.; Wang, Z.; Wu, Q. Scintillation properties of GAGG: Ce ceramic and single crystal. *Opt. Mat.* **2020**, *105*, 109964. [[CrossRef](#)]
- Korjik, M.; Bondarau, A.; Dosovitskiy, G.; Dubov, V.; Gordienko, K.; Karpuk, P.; Komendo, I.; Kuznetsova, D.; Mechinsky, V.; Pustovarov, V.; et al. Lanthanoid-doped quaternary garnets as phosphors for high brightness cathodoluminescence-based light sources. *Heliyon* **2022**, *8*, E10193. [[CrossRef](#)] [[PubMed](#)]

17. Korzhik, M.; Borisevich, A.; Fedorov, A.; Gordienko, E.; Karpyuk, P.; Dubov, V.; Sokolov, P.; Mikhlin, A.; Dosovitskiy, G.; Mechinsky, V.; et al. The scintillation mechanisms in Ce and Tb doped $(\text{Gd}_x\text{Y}_{1-x})\text{Al}_2\text{Ga}_3\text{O}_{12}$ quaternary garnet structure crystalline ceramics. *J. Lumin.* **2021**, *234*, 117933. [[CrossRef](#)]
18. Korzhik, M.; Abashev, R.; Fedorov, A.; Dosovitskiy, G.; Gordienko, E.; Kamenskikh, I.; Kazlou, D.; Kuznecova, D.; Mechinsky, V.; Pustovarov, V.; et al. Towards effective indirect radioisotope energy converters with bright and radiation hard scintillators of $(\text{Gd},\text{Y})_3\text{Al}_2\text{Ga}_3\text{O}_{12}$ family. *Nucl. Eng. Technol.* **2022**, *54*, 2579–2585. [[CrossRef](#)]
19. Dujardin, C.; Auffray, E.; Bourret, E.; Dorenbos, P.; Lecoq, P.; Nikl, M.; Vasil'ev, A.N.; Yoshikawa, A.; Zhu, R. Needs, trends, and advances in inorganic scintillators. *IEEE Trans. Nucl. Sci.* **2018**, *65*, 1977–1997. [[CrossRef](#)]
20. Tian, F.; Ikesue, A.; Li, J. Progress and perspectives on composite laser ceramics: A review. *J. Eur. Ceram. Soc.* **2022**, *42*, 1833–1851. [[CrossRef](#)]
21. Ievlev, V.M.; Putlyaev, V.I.; Safronova, T.V.; Evdokimov, P.V. Additive technologies for making highly permeable inorganic materials with tailored morphological architectonics for medicine. *Inorg. Mater.* **2015**, *51*, 1297–1315. [[CrossRef](#)]
22. Zocca, A.; Colombo, P.; Gomes, C.M.; Günster, J. Additive manufacturing of ceramics: Issues, potentialities, and opportunities. *J. Am. Ceram. Soc.* **2015**, *98*, 1983–2001. [[CrossRef](#)]
23. Travitzky, N.; Bonet, A.; Dermeik, B.; Fey, T.; Filbert-Demut, I.; Schlier, L.; Schloridt, T.; Greil, P. Additive manufacturing of ceramic-based materials. *Adv. Eng. Mater.* **2014**, *16*, 729–754. [[CrossRef](#)]
24. Fedorov, A.A.; Dubov, V.V.; Ermakova, L.V.; Bondarev, A.G.; Karpyuk, P.V.; Korzhik, M.V.; Kuznetsova, D.E.; Mechinsky, V.A.; Smyslova, V.G.; Dosovitskiy, G.A.; et al. $\text{Gd}_3\text{Al}_2\text{Ga}_3\text{O}_{12}:\text{Ce}$: Scintillation ceramic elements for measuring ionizing radiation in gases and liquids. *Instrum. Exp. Tech.* **2023**, *2*, accepted.
25. Konstantinou, G.; Lecoq, P.; Benloch, J.M.; Gonzalez, A.J. Metascintillators for ultrafast gamma detectors: A review of current state and future perspectives. *IEEE Trans. Radiat. Plasma Med. Sci.* **2021**, *6*, 5–15. [[CrossRef](#)]
26. Pagano, F.; Kratochwil, N.; Salomoni, M.; Pizzichemi, M.; Paganoni, M.; Auffray, E. Advances in heterostructured scintillators: Toward a new generation of detectors for TOF-PET. *Phys. Med. Biol.* **2022**, *67*, 135010. [[CrossRef](#)] [[PubMed](#)]
27. Lecoq, P.; Konstantinou, G.; Latella, R.; Moliner, L.; Nuyts, J.; Zhang, L.; Gonzalez, A.J. Metascintillators: New results for TOF-PET applications. *IEEE Trans. Radiat. Plasma Med. Sci.* **2022**, *6*, 510–516. [[CrossRef](#)]
28. Yang, Y.; Liu, T.; Bi, L.; Deng, L. Recent advances in development of magnetic garnet thin films for applications in spintronics and photonics. *J. Alloys Compd.* **2021**, *860*, 158235. [[CrossRef](#)]
29. Telegin, A.; Sukhorukov, Y. Magnetic Semiconductors as Materials for Spintronics. *Magnetochemistry* **2022**, *8*, 173. [[CrossRef](#)]
30. Nemeth, Z.; Nomura, K.; Ito, Y. Room temperature ferromagnetism in dilute iron-doped yttrium aluminum garnet polycrystals. *J. Phys. Chem. C* **2009**, *113*, 20044–20049. [[CrossRef](#)]
31. Neupane, D.; Hulsebosch, L.; Ali, K.S.S.; Bhattarai, R.; Shen, X.; Pathak, A.K.; Mishra, S.R. Enhanced magnetocaloric effect in aluminum doped $\text{Gd}_3\text{Fe}_{5-x}\text{Al}_x\text{O}_{12}$ garnet: Structural, magnetic, and Mössbauer study. *Materialia* **2022**, *21*, 101301. [[CrossRef](#)]
32. Zhang, G.; Carloni, D.; Wu, Y. 3D printing of transparent YAG ceramics using copolymer-assisted slurry. *Ceram. Int.* **2020**, *46*, 17130–17134. [[CrossRef](#)]
33. Seeley, Z.; Yee, T.; Cherepy, N.; Drobshoff, A.; Herrera, O.; Ryerson, R.; Payne, S.A. 3D printed transparent ceramic YAG laser rods: Matching the core-clad refractive index. *Opt. Mat.* **2020**, *107*, 110121. [[CrossRef](#)]
34. Halloran, J.W. Ceramic stereolithography: Additive manufacturing for ceramics by photopolymerization. *Annu. Rev. Mater. Res.* **2016**, *46*, 19–40. [[CrossRef](#)]
35. Komissarenko, D.A.; Sokolov, P.S.; Evstigneeva, A.D.; Shmeleva, I.A.; Dosovitskiy, A.E. Rheological and curing behavior of acrylate-based suspensions for the DLP 3D printing of complex zirconia parts. *Materials* **2018**, *11*, 2350. [[CrossRef](#)] [[PubMed](#)]
36. Komissarenko, D.A.; Sokolov, P.S.; Evstigneeva, A.D.; Slyusar, I.V.; Nartov, A.S.; Volkov, P.A.; Lyskov, N.V.; Evdokimov, P.V.; Putlayev, V.I.; Dosovitskiy, A.E. DLP 3D printing of scandia-stabilized zirconia ceramics. *J. Eur. Ceram. Soc.* **2021**, *41*, 684–690. [[CrossRef](#)]
37. Sokolov, P.S.; Komissarenko, D.A.; Belus, S.K.; Dosovitskiy, G.A.; Kozlov, D.Y.; Dosovitskiy, A.E.; Korzhik, M.V. 3D printing of composite reflectors for enhanced light collection in scintillation detectors. *Opt. Mat.* **2020**, *108*, 110393. [[CrossRef](#)]
38. Li, Y.; Wang, M.; Wu, H.; He, F.; Chen, Y.; Wu, S. Cure behavior of colorful ZrO_2 suspensions during digital light processing (DLP) based stereolithography process. *J. Eur. Ceram. Soc.* **2019**, *39*, 4921–4927. [[CrossRef](#)]
39. Goldberg, M.; Obolkina, T.; Smirnov, S.; Protsenko, P.; Titov, D.; Antonova, O.; Konovalov, A.; Kudryavtsev, E.; Sviridova, I.; Kirsanova, V.; et al. The influence of Co additive on the sintering, mechanical properties, cytocompatibility, and digital light processing based stereolithography of 3Y-TZP-5Al₂O₃ ceramics. *Materials* **2020**, *13*, 2789. [[CrossRef](#)]
40. Fournier, S.; Chevalier, J.; Baeza, G.P.; Chaput, C.; Louradour, E.; Sainot, P.; Cavoret, J.; Reveron, H. Ceria-stabilized zirconia-based composites printed by stereolithography: Impact of the processing method on the ductile behaviour and its transformation features. *J. Eur. Ceram. Soc.* **2022**; in press. [[CrossRef](#)]
41. Inserra, B.; Coppola, B.; Montanaro, L.; Tulliani, J.-M.; Palmero, P. Preparation and characterization of Ce-ZrO₂/Al₂O₃ composites by DLP-based stereolithography. *J. Eur. Ceram. Soc.* **2022**; in press. [[CrossRef](#)]
42. Cailliet, S.; Roumanie, M.; Croux-Barghorn, C.; Bernard-Grager, G.; Laucournet, R. Y-TZP, Ce-TZP and as-synthesized Ce-TZP/Al₂O₃ materials in the development of high loading rate digital light processing formulations. *Ceram. Int.* **2021**, *47*, 3892–3900. [[CrossRef](#)]

43. Chang, J.; Zou, D.; Wang, X.; Yu, Y.; Chen, Q.; Zhang, G. The 3D printing and sintering preparation and coloring mechanism analysis of colorful ZrO₂ ceramics parts. *Mater. Today Commun.* 2022; *in press*. [[CrossRef](#)]
44. Hostaša, J.; Schwentenwein, M.; Toci, G.; Esposito, L.; Brouczek, D.; Piancastelli, A.; Pirri, A.; Patrizi, B.; Vannini, M.; Biasini, V. Transparent laser ceramics by stereolithography. *Scripta Mater.* **2020**, *187*, 194–196. [[CrossRef](#)]
45. Wang, T.; Zhang, J.; Zhang, N.; Wang, S.; Wu, B.; Jia, Z.; Tao, X. The characteristics of high-quality Yb: YAG single crystal fibers grown by a LHPG method and the effects of their discoloration. *RSC Adv.* **2019**, *9*, 22567–22575. [[CrossRef](#)] [[PubMed](#)]
46. Cooperstein, I.; Indukuri, S.R.K.C.; Boukvetov, A.; Levy, U.; Magdassi, S. 3D printing of micrometer-sized transparent ceramics with on-demand optical-gain properties. *Adv. Mat.* **2020**, *32*, 2001675. [[CrossRef](#)]
47. Kumar, G.A.; Lu, J.; Kaminskii, A.A.; Ueda, K.I.; Yagi, H.; Yanagitani, T. Spectroscopic and stimulated emission Characteristics of Nd³⁺ in transparent YAG ceramics. *IEEE J. Quantum Electron.* **2004**, *40*, 747–758. [[CrossRef](#)]
48. Dosovitskiy, G.A.; Karpyuk, P.V.; Evdokimov, P.V.; Kuznetsova, D.E.; Mechinsky, V.A.; Borisevich, A.E.; Fedorov, A.A.; Putlayev, V.I.; Dosovitskiy, A.E.; Korzhik, M.V. First 3D-printed complex inorganic polycrystalline scintillator. *CrystEngComm* **2017**, *19*, 4260–4264. [[CrossRef](#)]
49. Hu, S.; Liu, Y.; Zhang, Y.; Xue, Z.; Wang, Z.; Zhou, G.; Lu, C.; Li, H.; Wang, S. 3D printed ceramic phosphor and the photoluminescence property under blue laser excitation. *J. Eur. Ceram. Soc.* **2019**, *39*, 2731–2738. [[CrossRef](#)]
50. Ueda, J.; Tanabe, S. Review of luminescent properties of Ce³⁺-doped garnet phosphors: New insight into the effect of crystal and electronic structure. *Opt. Mat. X* **2019**, *1*, 100018. [[CrossRef](#)]
51. Li, J.G.; Ikegami, T.; Lee, J.H.; Mori, T. Low-temperature fabrication of transparent yttrium aluminum garnet (YAG) ceramics without additives. *J. Am. Ceram. Soc.* **2000**, *83*, 961–963. [[CrossRef](#)]
52. Zhou, D.; Qi, H.; Zhou, B.; Wang, Y.; Zhou, Z.; Wang, L.; Xu, J.; Shi, Y. Mixed precipitants derived nanocrystalline powders and RE doped LuAG transparent ceramics. *Ceram. Int.* **2022**, *48*, 24788–24792. [[CrossRef](#)]
53. Xu, X.; Sun, X.; Liu, H.; Li, J.G.; Li, X.; Huo, D.; Liu, S. Synthesis of monodispersed spherical yttrium aluminum garnet (YAG) powders by a homogeneous precipitation method. *J. Am. Ceram. Soc.* **2012**, *95*, 3821–3826. [[CrossRef](#)]
54. Karpyuk, P.V.; Dosovitskiy, G.A.; Kuznetsova, D.E.; Gordienko, E.V.; Fedorov, A.A.; Mechinsky, V.A.; Dosovitskiy, A.E.; Korzhik, M.V. Ceramic scintillation materials—Approaches, challenges and possibilities. In *Engineering of Scintillation Materials and Radiation Technologies. ISMART 2018*; Korzhik, M., Gektin, A., Eds.; Springer Proceedings in Physics; Springer: Cham, Switzerland, 2019; Volume 227, pp. 57–74. [[CrossRef](#)]
55. Klee, J.E.; Maier, M.; Fic, C.P. Applied Photochemistry in Dental Materials: From Beginnings to State of the Art. In *Dyes and Chromophores in Polymer Science*; Lalevée, J., Fouassier, J.-P., Eds.; Wiley: Hoboken, NJ, USA, 2015. [[CrossRef](#)]

Disclaimer/Publisher’s Note: The statements, opinions and data contained in all publications are solely those of the individual author(s) and contributor(s) and not of MDPI and/or the editor(s). MDPI and/or the editor(s) disclaim responsibility for any injury to people or property resulting from any ideas, methods, instructions or products referred to in the content.